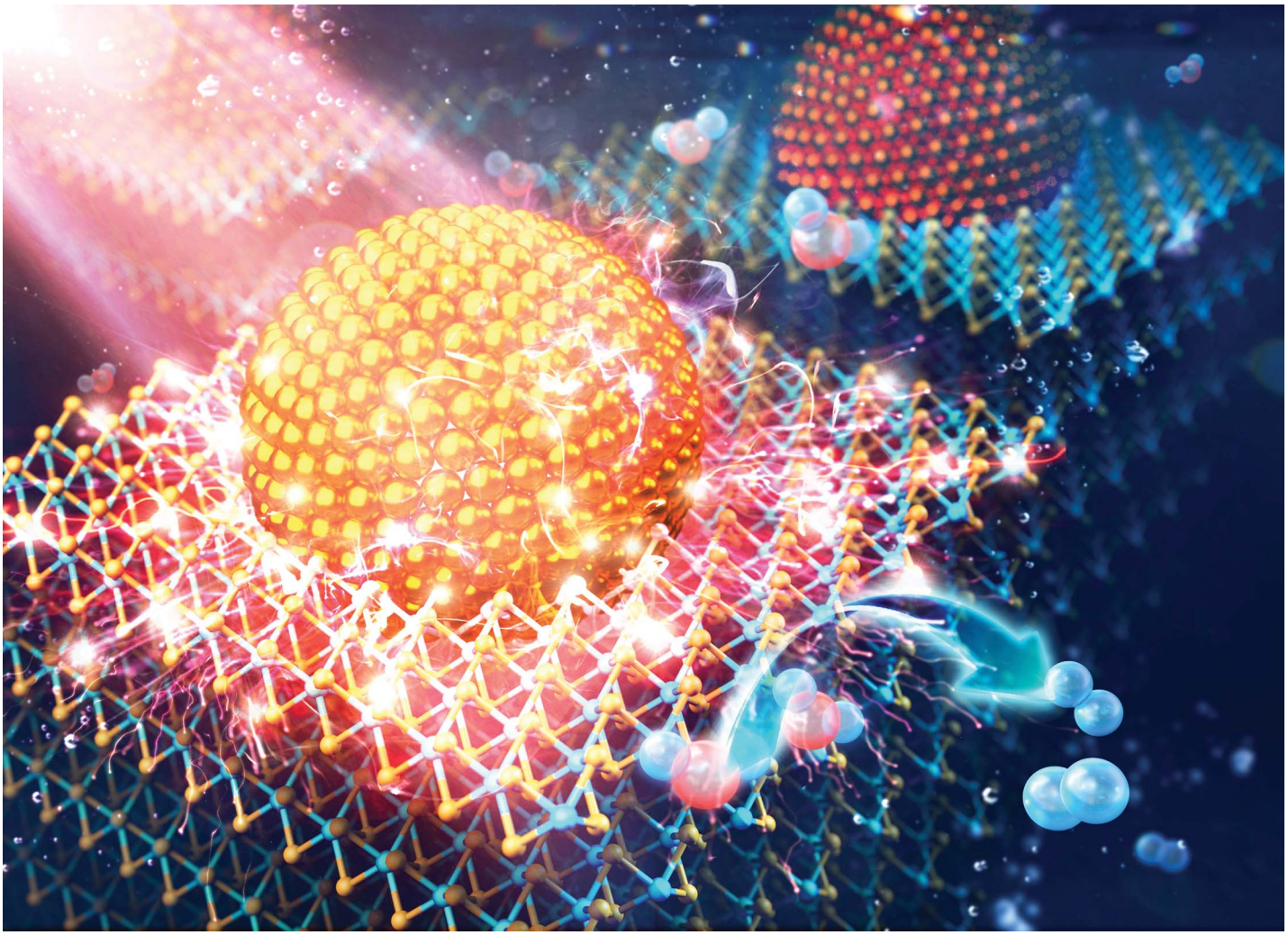

Showcasing a study on the Au-FeS_2 heterostructure photocatalyst and their application in photoelectrocatalytic water reduction by a group of researchers led by Prof. Jeong Y. Park from Department of Chemistry, KAIST and Center for Nanomaterials and Chemical Reaction, Institute for Basic Sciences.

Two-dimensional FeS_2-encapsulated Au: a quasi-epitaxial heterojunction for synergistic catalytic activity under photoelectrocatalytic water reduction

Two-dimensional thin FeS_2 and its analogue Au heterostructures were synthesized with a hot-injection method. The Au-FeS_2 heterostructure photocatalyst showed highly improved cathodic performance compared with bare FeS_2. This study demonstrates the synergistic effect of the generation of hot electrons on Au and fast charge flow across the FeS_2 layer.

As featured in:

See Jeong Young Park *et al.*, *J. Mater. Chem. A*, 2019, **7**, 19258.

ROYAL SOCIETY OF CHEMISTRY | Celebrating IYPT 2019

rsc.li/materials-a

Registered charity number: 207890

Published on 27 June 2019. Downloaded by Korea Advanced Institute of Science & Technology / KAIST on 1/16/2020 12:43:40 AM.

Journal of Materials Chemistry A

PAPER

View Article Online
View Journal | View Issue

Check for updates

Cite this: J. Mater. Chem. A, 2019, 7, 19258

Two-dimensional FeS_2-encapsulated Au: a quasi-epitaxial heterojunction for synergistic catalytic activity under photoelectrocatalytic water reduction†

Indranil Mondal,[a] Song Yi Moon,[b] Hyunhwa Lee,[b] Heeyoung Kim[b] and Jeong Young Park *[ab]

Received 24th February 2019
Accepted 24th June 2019

DOI: 10.1039/c9ta02065a

rsc.li/materials-a

We report the development of two-dimensional pyrite-type FeS_2 nanosheets with tunable bulk size controlled by sulfide-mediated thermal diffusion under inert atmosphere. We also synthesized Au heterostructures that are encapsulated by FeS_2, where the sulfide concentration and annealing time lead to eccentric aggregation of the FeS_2. p-type Si coupled with the as-prepared catalysts exhibited enhanced photocathodic performance under an acidic medium. With FeS_2, the optimized photocathodic performance was obtained by achieving a geometric photocurrent of 10 mA cm^{-2} at a positive applied potential of 0.08 V (*vs.* reversible hydrogen electrode (RHE)). As the size of the FeS_2 increased, the cathodic photocurrent also increased, which indicates a longer carrier lifetime and slow charge recombination on the catalyst surface. It was found that the direction of the FeS_2 growth is aligned with the equivalent (111) plane of the Au, resulting in a unique Au–FeS_2 heterostructure. The optimized heterostructure photocatalyst showed highly improved cathodic performance with an anodic shift of the cell voltage by 0.26 V (*vs.* RHE) compared with bare FeS_2. This study demonstrates the synergistic effect of the generation of hot electrons on Au and fast charge flow across the FeS_2 layer, which facilitates fast electron–hole separation and enhances the hydrogen evolution reaction.

Introduction

Molecular hydrogen generation by means of solar water electrolysis is presently at the forefront for renewable energy conversion.[1–5] The efficiency of a solar water-splitting system depends on the structural and electronic features of the catalyst, as well as on the compatibility of the catalysts and light absorbers in an integrated system.[6] These factors invariably control the kinetics of electron transfer at the electrode/electrolyte interface and the overpotential requirement.[7] In a photoelectrochemical (PEC) water-splitting cell, the choice of absorber and its suitable configuration with a counter catalyst can also essentially compensate for free energy losses, modeling losses, kinetic losses, *etc.*[8] Certainly, Si-based PEC devices (modified with an electrocatalyst) are under intense focus because of the suitable photonic and electric behaviors of Si as an intrinsic semiconducting circuit element in a wide variety of PEC units.[9] The electrocatalyst also provides a passivated environment that preserves Si from surface oxidation when under an electrolyte medium.[10,11] Although current research efforts to fabricate a stable and efficient Si photoelectrode continue to provide interesting observations, the strategy for using an electrocatalyst to utilize the majority of the donor density in a Si-based electrode device has only received sporadic attention.

Owing to the flexible oxidation state of the metal center and the tunable proton-binding active surface sites, transition-metal chalcogenide electrocatalysts are of high interest for replacing Pt-group metals for water splitting.[12–17] Moreover, by virtue of contributing to the partially filled e_g band for spanning the Fermi level, transition metal chalcogenides are very beneficial in a wide variety of electrocatalytic reactions.[18] With this added advantage and having tunable physico-chemical properties, layered two-dimensional (2D) nanostructured catalysts are being developed at a rapid pace for water splitting.[19–21] Furthermore, unlike nonmetal–metal–nonmetal layers in 2D layered transition-metal dichalcogenides, the family of cubic pyrite-type or orthorhombic marcasite-type structures features octahedrally bonded metal with adjacent chalcogen atoms.[22] However, the implementation of metal chalcogenides – especially sulfides – is hardly known because of inconsistent behavior from mass activities and unidentified *iR* loss.

[a]Center for Nanomaterials and Chemical Reactions, Institute for Basic Science (IBS), Daejeon 305-701, Republic of Korea

[b]Department of Chemistry, Korea Advanced Institute of Science and Technology (KAIST), Daejeon, 305-701, Republic of Korea. E-mail: jeongypark@kaist.ac.kr

† Electronic supplementary information (ESI) available. See DOI: 10.1039/c9ta02065a

This journal is © The Royal Society of Chemistry 2019

Published on 27 June 2019. Downloaded by Korea Advanced Institute of Science & Technology / KAIST on 1/16/2020 12:43:40 AM.

Although metal sulfides, *e.g.*, molybdenum sulfide,[23] cobalt sulfide,[24,25] copper sulfide,[26,27] nickel sulfide,[28,29] tungsten disulfide,[30] are good candidates as cocatalysts for water splitting, FeS_2 (or FeS) is rarely used for photocatalytic activity. Tabata *et al.* demonstrated the superiority of FeS as a cocatalyst when in physical contact with copper gallium sulfide.[31] There are a number of reports of comprehensive studies of the electrocatalytic activity of pyrite-type FeS_2 and their active sites (or species) in a reaction medium.[32–36] For instance, Giovanni *et al.* explored the role of biomimetic Fe/S clusters in disk-like pyrite FeS_2 for the hydrogen evolution reaction (HER).[32] Leonard and co-workers first demonstrated the electrocatalytic activity of thin pyrite FeS_2 and the role of dimensionality with varied performance.[33] Moreover, three-dimensional mesoporous structures have also proved to be proficient candidates for the same activity.[34] Certainly, this provides motivation to synthesize a metal-rich (featuring n-type characteristics) pyrite FeS_2 where more open active sites could be controlled by constrained growth and the promotion of photoexcited electrons, which currently remain unexplored.

The use of surface plasmon resonance to inject hot electrons into an electrocatalyst layer is an interesting approach for synergizing water splitting activity. There are very few studies exploring where plasmon-induced hot electrons are used by electrocatalysts, *i.e.*, either directly to the reaction site or by stimulating the active species of the catalyst.[37–39] Moreover, plasmon-induced hot electrons can be injected into the FeS_2 layer because of the low Schottky energy barrier between the FeS_2 and the Au and because the energy levels match.[40] This encourages us to fabricate a plasmonic nanostructure/electrocatalyst heterojunction system that can pull electrons from the light absorber while providing trapping sites for the photo-excited electrons from the Si and suppress electron–hole recombination during the water reduction reaction.

Pyrite-type FeS_2 with different lateral sizes and modulated heterostructures with plasmonic Au (Au–FeS_2) were exploited here as efficient photocathode electrocatalyst materials for PEC water splitting. The nature of the lateral FeS_2 growth and its hetero epitaxial relationship with Au were investigated by changing the S^{2-} concentration. The n-type FeS_2 and Au–FeS_2 enables a p–n type heterojunction while deposited atop Si, which acts as the light absorber. The resulting photocathode delivers a different activity depending on the controlled growth, aggregation, and electronic features. The maximum cathodic sweep was obtained when achieving a standard current density of 10 mA cm^{-2} at 0.34 V of applied bias. To the best of our knowledge, this is the highest performance reported to date among sulfide-based electrocatalysts measured on p-type Si.

Results and discussion

The adopted hot-injection method resembles earlier studies for synthesizing size- and shape-controlled metal sulfide nanocrystals.[41,42] The gradual 2D growth of FeS_2 was the result of digesting 0.1 mmol of Fe salt [$Fe(acac)_3$] in a closed reaction flask along with the coordinating reducing solvent dodecylamine (DDA) and a suitable amount of trioctylphosphine followed by the injection of the S precursor (thiourea) at 170 °C under inert atmosphere. In the first step of the synthesis, DDA reduced the Fe^{3+} and formed a capping layer on the Fe^0 seed, which was oxidized in the presence of S^{2-} in the next step to form FeS_2, which is black. S^{2-} was generated *in situ* from thermolysis of thiourea in the presence of DDA. The mechanism involved in the elementary steps with long-chain amines was previously reported.[43,44] Thus, the most plausible reaction pathway is depicted in Scheme 1.

Different pyrite FeS_2 nanostructures synthesized using 0.5, 1.5, and 2.5 mmol of thiourea are labelled FS0.5, FS1.5, and FS2.5, respectively. Both the size and shape of the 2D structure changed as the injected S^{2-} concentration changed. At a Fe : S ratio of 1 : 5 (*i.e.*, FS0.5), thin disk-like FeS_2 structures were obtained with an average size of 200 nm that were partially stacked on each other and the (200) plane was predominantly exposed (Fig. 1a). As the S^{2-} concentration increased to a Fe : S ratio of 1 : 15 (*i.e.*, FS1.5), the FeS_2 underwent more growth with non-uniform aggregation (Fig. 1b). Eventually, a thin nanosheet (1–5 nm) forms (Fig. 1c) that features micron to submicron lateral growth at a Fe : S ratio of 1 : 25 (*i.e.*, FS2.5). Shrinkage in the nanosheet appeared in FS1.5 and showed a prominent bending that resembles the flake-like structures in FS2.5. Atomic force microscopy (AFM) analysis of the FS2.5 was performed on a clean Si substrate using non-contact mode. The step height extracted from the line scanning shown in the AFM topography is estimated to be 3–4 nm, which is attributed to a few layers of FeS_2 aggregation (Fig. S1†). The results are consistent with the observations from the scanning electron microscopic (SEM) images. A possible reason for the high lateral growth of the FeS_2 is the formation of constant Fe nuclei that take part in the growth of more monomers at the higher S^{2-} concentration.

The exterior of the FS2.5 can be seen from the top and cross-section views of the SEM image of the catalyst ink deposited on the Si surface (the detailed method for deposition is discussed in the experimental section). The thin and ruffled edge surface of the FS2.5 nanosheet can be seen in Fig. S2.† While the photocatalytic activity was considered, this class of sheet-like structures is highly beneficial because it has more active sites

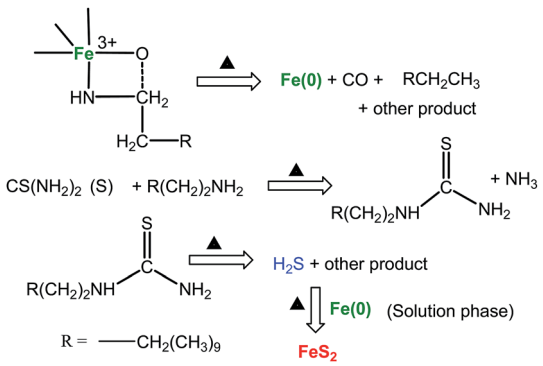

Scheme 1 Plausible reaction pathway for the formation of Fe(0) *via* an intermediate complex with DDA and *in situ* generation of H_2S from thiourea, which helps to oxidize Fe(0) to pyrite FeS_2.

Published on 27 June 2019. Downloaded by Korea Advanced Institute of Science & Technology / KAIST on 1/16/2020 12:43:40 AM.

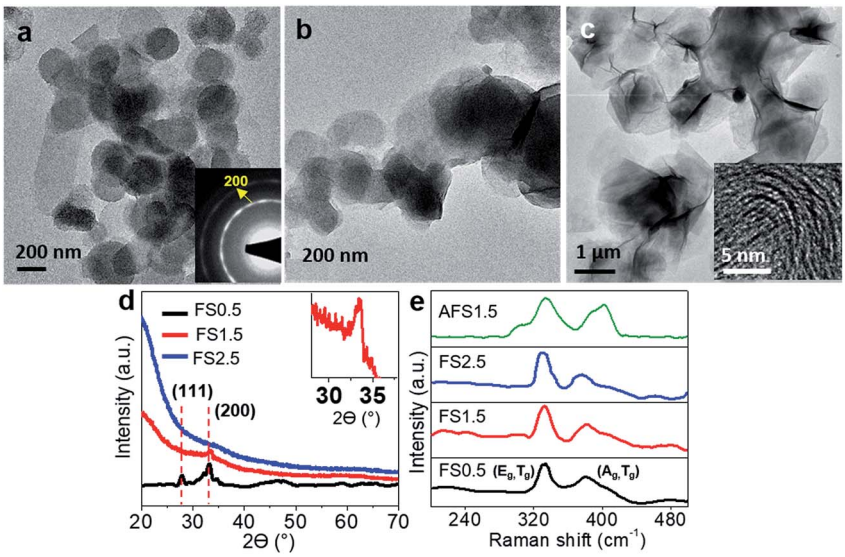

Fig. 1 Low-magnification TEM images of FeS_2 synthesized using (a) 0.5 mmol of S^{2-} (FS0.5) (inset shows the ring diffraction pattern for the (200) plane of pyrite FeS_2), (b) 1.5 mmol of S^{2-} (FS1.5), and (c) 2.5 mmol of S^{2-} (FS2.5) (inset shows shrinkage in the flake-like nanostructure). (d) Powder XRD pattern of the different FeS_2 (inset shows high-magnification pattern of FS1.5, which has a very low intensity peak at 33°). (e) Raman spectra of all the FeS_2 and representative Au–FeS_2 catalysts.

and a short carrier diffusion length.[45] Initially, powder X-ray diffraction (XRD) was carried out to detect the phase of the as-synthesized FeS_2 (Fig. 1d). FS0.5 shows very low intense peaks at 27.5° and 33°, which can be indexed to the (111) and (200) planes, respectively, of the pyrite phase (JCPDS no. 42-1340). A trace of the (200) plane was also found in the XRD pattern for FS1.5, but this plane did not appear in the XRD pattern for FS2.5. This is caused by the amorphous nature and very low thickness of the FeS_2 materials, which leads to an inadequate scattering volume.[33] To further confirm the phase, Raman spectra of the FeS_2 catalysts were collected that showed the characteristic (E_g, T_g) and (A_g, T_g) bands at 320–352 and 370–414 cm^{-1}, respectively, that are attributed to pyrite FeS_2 (Fig. 1e).[46] The optical properties were investigated by collecting UV-Vis diffuse reflectance spectra and the band gaps (using the Tauc plot) are estimated as 0.82, 0.77, and 0.71 eV for the FS0.5, FS1.5, and FS2.5, respectively (Fig. S3†). A slight decrease in the band gap is likely caused by the increase in the thickness of the overgrown FeS_2 sheet.[47]

In the following study, a modulated Au–FeS_2 heterostructure was synthesized by adjusting the Au precursor (0.05 mmol $HAuCl_4$) injected just after the nucleation of the FeS_2 and by freezing the reaction after 3 min of annealing. The isolation time of the final products correlated with their respective structural features and electrocatalytic activity, which is discussed later. $HAuCl_4$ was not added in the reaction mixture before injecting the sulfur precursor to avoid any bimetallic nucleation between the Fe and the Au.[48] As the concentration of the S^{2-} increased following the same trend as employed earlier, the FeS_2 exhibited a varied amount of lateral growth centered on the Au (Fig. S4†). In this regard, the Au–FeS_2 nanostructures prepared using 0.5, 1.5, and 2.5 mmol of thiourea are labelled AFS0.5, AFS1.5, and AFS2.5, respectively.

The XRD only showed the peaks of fcc Au (Fig. S5†), but the phase of the FeS_2 in the Au–FeS_2 heterostructure can be detected using Raman spectra, which has a pattern identical to pure FeS_2 (Fig. 1e). Notably, the intensity of the T_g mode increased slightly, which may be the result of the change in local strain caused by the inclusion of Au.[49] The mutual attachment between the Au and the FeS_2 was understood using elemental mapping of Au, Fe, and S, that was collected within the selected area high-angle annular dark-field scanning transmission electron microscopy (HAADF-STEM) image of AFS1.5 (Fig. S6†). The Au nanoparticle primarily holds the core position in the Au–FeS_2 heterojunction. It is worth pointing out that the lateral growth of FeS_2 around the Au particle did not significantly increase with increased S^{2-} concentration, rather it showed an overgrowth that enveloped the Au center. The stacking of the FeS_2 can be understood from the corresponding HAADF-STEM image (Fig. S4,† inset). To get a clear understanding of the epitaxial relation between the Au and the FeS_2 heterostructure, a high-resolution TEM (HRTEM) nanograph and corresponding fast Fourier transform (FFT) image were analyzed for the AFS1.5 and AFS2.5 as representative nanostructures. Fig. 2a and b shows the typical heterojunction between the Au and FeS_2 in AFS1.5 and the corresponding lattice fringes were identified using HRTEM (Fig. 2c). The characteristic orientations of the (200) and (211) planes, which have corresponding lattice distances of 0.28 and 0.23 nm, respectively, also affirm the presence of pyrite FeS_2. The respective FFT patterns extracted from the area displayed in Fig. 2c (shown in Fig. 2d) indicate the epitaxial relation between the fcc Au and pyrite FeS_2 along their viewing direction. The atomic model was designed based on the FFT analysis (Fig. 2e), where the Au (−111) plane could coincide with the FeS_2 (210) plane that has close lattice *d*-spacing. The line profile of the selected nanostructure confirms that the

 This journal is © The Royal Society of Chemistry 2019

Published on 27 June 2019. Downloaded by Korea Advanced Institute of Science & Technology / KAIST on 1/16/2020 12:43:40 AM.

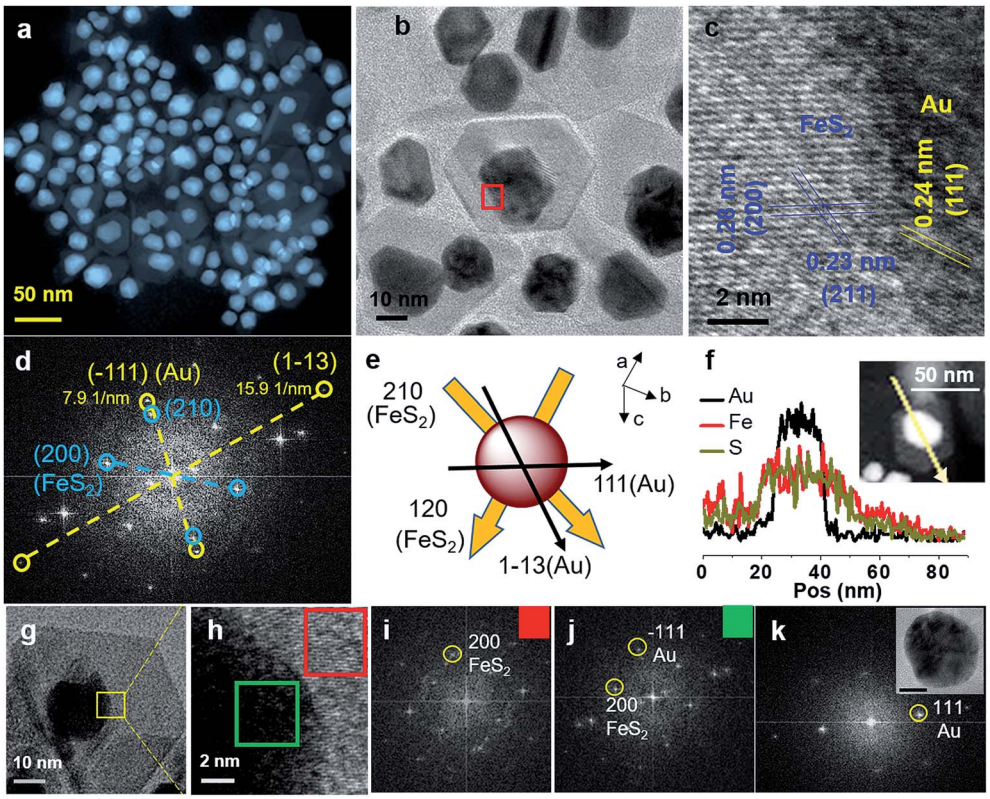

Fig. 2 TEM analysis of the Au–FeS_2 heterostructure prepared using 1.5 mmol of S^{2-} (AFS1.5). (a) Low- (HAADF-STEM) and (b) high-magnification TEM images. (c) HRTEM of the selected area marked with the red box in (b). (d) FFT pattern collected from the HRTEM image. (e) Atomic model showing the attachment of Au and FeS_2 along the respective viewing directions with their exposed planes. (f) STEM-EDX line profile of the selected area shown in the inset image. (g) High-magnification TEM image of another selected position on AFS1.5 and (h) corresponding HRTEM image. FFT pattern from the (i) red and (j) green boxes in (h). (k) FFT pattern of the Au nanoparticle shown in the inset (scale 5 nm).

high-density Au core is confined by the FeS_2, which did not show any visible aggregation around the Au particle (Fig. 2f). The orientation between the Au and FeS_2 is found to be analogous throughout the sample, as confirmed by additional FFT analysis of the selected area captured from a different position on the AFS1.5. The FFT pattern collected from the top of the Au nanoparticle (Fig. 2j, green label) is similar to the pattern shown in Fig. 2d, which is clearly distinguishable from the FFT of the bare FeS_2 (Fig. 2i, area labeled in red). As a control, the FFT of the bare fcc Au nanoparticle (synthesized using the same procedure as for the AFS1.5 without the Fe or S precursor) was also compared with the heterojunction. The results indicate the presence of a few layers of FeS_2 on the Au nanoparticle, as corroborated by the line profile analysis. On the other hand, the Au–FeS_2 heterostructure synthesized at the higher S^{2-} concentration (AFS2.5) showed high-density FeS_2 around the Au nanoparticle, where the size of the Au is a little larger in some distinct positions (Fig. 3a). Like AFS1.5, the (200) facet of the FeS_2 was mostly exposed and enveloped the Au surface (Fig. 3b). From the HAADF-STEM analysis and its corresponding line profile, it is clear that unlike AFS1.5, the FeS_2 has a distinguishable higher overgrowth in some positions (Fig. 3c and d). Fig. 3e shows the selected-area FFT analysis of the Au and FeS_2, which indicates nonselective precipitation of AFS2.5 (unlike AFS1.5) on the grid; to better reveal this detail, additional FFT analysis was performed using a different region of the AFS2.5 where the FeS_2 growth is very thin. The captured area shown in Fig. S7,† exhibits clear (210) and (−111) facets of pyrite FeS_2 and fcc Au, which are similar to the structure of AFS1.5. During the synthesis of Au–FeS_2 using different Fe : S ratios, it is expected that there was thermal fusion of the appropriate lattice planes after the formation of both materials[50,51] where the sulfide ion plays a significant role. It could be assumed that a thin atomic layer of gold sulfide is formed as the intermediate, which helped the Au(0) to diffuse on the FeS_2 sheet. Notably, the gas-phase (*in situ* formed H_2S) concentration is higher at higher S^{2-} concentrations.[44] In this case, the size of the Au nanoparticle could be a little larger to rationalize the epitaxial growth.[51] The distribution curve for the size of the Au nanoparticles extracted from the TEM analysis is incorporated in Fig. S4.† The surface and subsurface ionic states of the as-prepared FeS_2 and Au–FeS_2 nanostructure (FS1.5 and AFS1.5 as representative samples) were detected using XPS. The binding energies were calculated using C 1s as the reference. As shown in Fig. S8a and c,† the deconvoluted Fe $2p_{3/2}$ XPS profile predominantly consists of Fe^{2+} with characteristic BE values of 706.92 and 706.91 eV for FeS_2 and Au–FeS_2, respectively. This is consistent with Fe^{2+} bound to S as S_2^{2-} rather than S^{2-}.[52] The measured spin–orbit

Published on 27 June 2019. Downloaded by Korea Advanced Institute of Science & Technology / KAIST on 1/16/2020 12:43:40 AM.

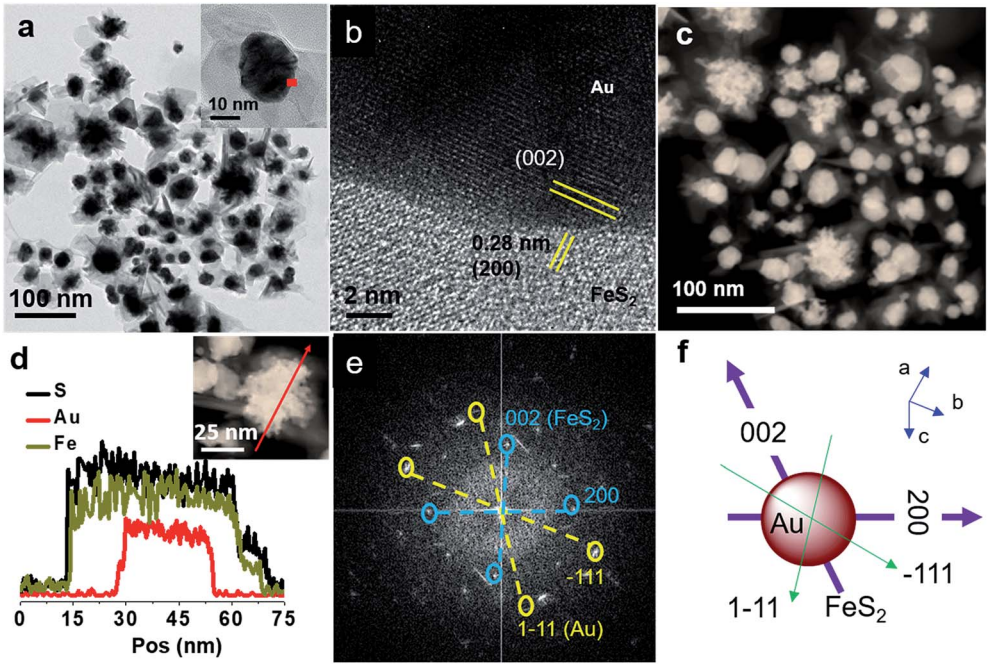

Fig. 3 TEM analysis of the Au–FeS_2 heterostructure prepared using 2.5 mmol of S^{2-} (AFS2.5). (a) Low-magnification TEM image (with high-magnification image in the inset), (b) HRTEM of selected area marked with red box in the inset of (a), (c) HAADF-STEM image, (d) STEM-EDX line profile of the selected area shown in the inset image, (e) as-obtained FFT image of the HRTEM profile shown in (b), and (f) schematic atomic model of the Au and FeS_2 based on their mutual configuration.

splitting between Fe $2p_{3/2}$ and Fe $2p_{1/2}$ is 13.2 eV. The slight distinguishable broad peaks around 710.7 eV in these samples possibly indicate the presence of small amounts of FeOOH.[52] On the other hand, fitting the XPS spectrum of the S 2p peaks indicates two auxiliary sulfur species apart from bulk S_2^{2-} at 160.9 and 162 eV, which are outer surface S_2^{2-} (appearing at 160.4–161.1 eV) and satellite sulfur species (162.8–164.4 eV), respectively, within the S $2p_{3/2}$. This is very consistent with the oxidation state of S in the natural pyrite phase.[53] The peaks in the region of 167.3–168.8 eV (attributed to surface sulfates (SO_4^{2-})) are caused by exposure to air.

A standard three-electrode configuration was employed to measure the photocathodic performance of the different Si (p-type)/FeS_2 (or Au–FeS_2) electrodes in an Ar-saturated 0.2 M H_2SO_4 solution at a scan rate of 10 mV s^{-1} at room temperature. All the experiments were performed using a Ag/AgCl reference electrode and the potentials are expressed with respect to a reference hydrogen electrode (RHE).[6] Cut p-type Si was initially treated in a 5% aqueous HF acid solution with ultrasonication for 1 min to remove the native oxide layer. Given an applied potential of −0.6 V, bare p-type Si can generate a 10 mA cm^{-2} photocurrent with an onset potential, *i.e.*, potential where the photocurrent reaches 10 μA cm^{-2}, of 0.02 V (Fig. S9†). Before deposition onto the Si surface, the as-prepared FeS_2 and Au–FeS_2 samples were treated with a *N*,*N*′ dimethylformamide solution containing Na_2S, which uncaps the hydrophobic alkyl chain ligand. This step is necessary for making the nanoparticles hydrophilic.[54] Before fabrication of the electrodes, the catalyst ink (with <0.5 mg catalyst) was drop casted on the Si surface and annealed at 150 °C for 1 h. The exterior of the FS2.5 deposited Si exhibits a catalyst layer of approximately 800 nm to 1 μm (Fig. S2†). It is worth mentioning here that the cocatalyst layer atop the electrode surface should be moderate so that it can balance the desired transparency *versus* the unwanted loss of activity caused by the thin catalyst layer.[55] When testing the FS2.5/Si electrode, the current density increased substantially in the presence of light (Fig. S9†). The same electrode showed a significant difference in the overpotential (0.68 V for generating 10 mA cm^{-2}) in comparison with bare Si. Among the different FeS_2 electrocatalysts, FS2.5 manifested the best performance, achieving a geometric current density of 10 mA cm^{-2} at 0.08 V with a positive onset potential of 0.4 V. FS0.5 and FS1.5 acquired higher overpotentials of 0.18 and 0.09 V, respectively, in comparison with FS2.5 at 10 mA cm^{-2} (Fig. 4a). Moreover, the FS0.5 (0.26) and FS1.5 (0.35) have lower estimated fill factor values compared with FS2.5 (0.52),[56] which may be caused by sluggish electron transport kinetics and intrinsic ohmic losses at the higher operating potentials.[57–59] To further clarify the activity of the FS2.5 deposited Si, the performance of the FS2.5/fluorine-doped tin oxide (FTO) was also recorded under light irradiation. The requirement of a high driving force (at a cell voltage −0.75 V) for the bare FS2.5 to generate a 10 mA cm^{-2} current is much inferior to model Si/FeS_2 electrodes. On the other hand, the Au–FeS_2 heterostructures generated current density with much smaller cell voltages and most of the Au–FeS_2/Si electrodes reached an adequate current density to form H_2 gas bubbles at the thermodynamic potential of H^+/H_2. The recorded current density value is sufficiently reproducible as

 This journal is © The Royal Society of Chemistry 2019

Published on 27 June 2019. Downloaded by Korea Advanced Institute of Science & Technology / KAIST on 1/16/2020 12:43:40 AM.

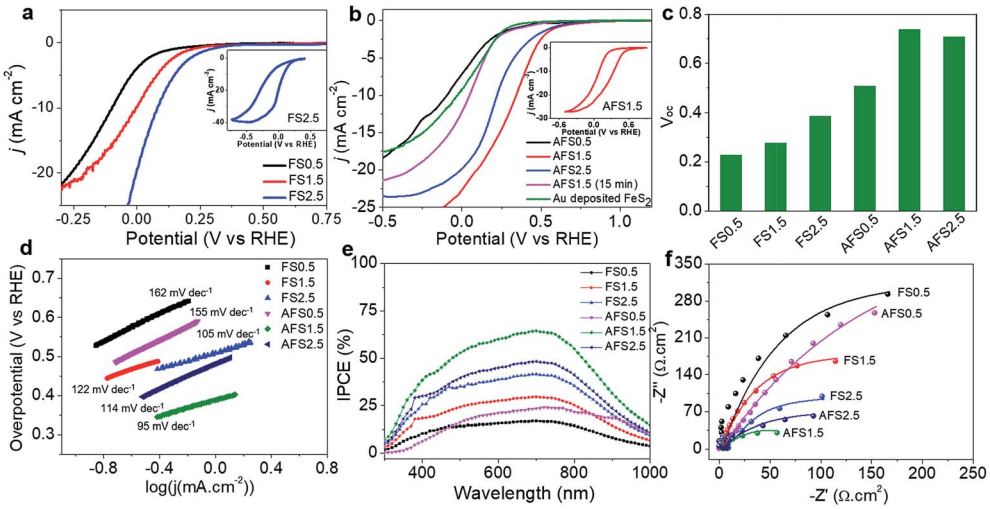

Fig. 4 Typical I–V curves of (a) the different Si/FeS_2 (inset: full scan CV of FS2.5) and (b) the Si/Au–FeS_2 photocathodes (inset: full scan CV of the AFS1.5), (c) open circuit potential values of the different catalysts, (d) Tafel polarization plot of the corresponding photoanodic performance for the different catalysts, (e) IPCE plot for the different Si/FeS_2 and Au–FeS_2 photocathodes at the chronoamperometric condition of 0 V. The corresponding IPCE was measured using IPCE(η) = (hcI)/(λJ_{light}), where I is the measured photocurrent density, J_{light} is the irradiance power at a specific wavelength, λ is the incident light wavelength, h is the Planck constant, and c is the speed of light. (f) Nyquist impedance plots of the different Si/FeS_2 and Au–FeS_2 photocathodes under light (the colored lines show the fitted curves).

confirmed by multiple CV scans of the Au–FeS_2 (AFS1.5)/Si electrode (Fig. S10†). The comprehensive screening shows that AFS1.5 is the optimized catalyst, generating a current density of 10 mA cm^{-2} at an applied bias of 0.34 V that was initialized with a positive onset potential of 0.8 V (Fig. 4b). Interestingly, AFS2.5, which was synthesized at a higher S^{2-} concentration, performed poorly in comparison with AFS1.5; AFS2.5 reached the same current (10 mA cm^{-2}) at 0.22 V. In contrast, the Au-deposited FeS_2 sheet (Fig. S11†) was much less active compared with AFS1.5; it followed a I–V relation similar to that of AFS0.5 (Fig. 4b). This is attributed to the beneficial role of the Au–FeS_2 heterojunction prepared using the hot-injection method over conventional Au/FeS_2 composites where Au is only in physical contact with the FeS_2. The faradaic efficiency calculated from the yields of both gases is more than 95% (Fig. S12†), indicating that the charge generated on the AFS1.5/Si photocathode is almost fully consumed during the water reduction reaction. Fig. 4c presents a plot of the open circuit potentials (V_{oc}) under illumination for a number of samples, which clearly indicate that the FS2.5 and AFS1.5 show a considerable anodic shift in the onset potential as compared to their analogues. Moreover, to understand the rate-limiting step of the HER, the Tafel plot was recorded after adding the quasi-Fermi level potential of the p-type Si to the overpotential for the various catalysts and fitted according to the Tafel equation (Fig. 4d). The slope was evaluated from the linear region of the curve. The smaller Tafel slope of AFS1.5 (95 mV dec^{-1}) is attributed to an increasing reaction rate with increasing overpotential. It is worth noting here that the Au–FeS_2 heterostructures were isolated at 3 min to retain the plasmonic Au character and to avoid over-growth of the FeS_2. Within 3 minutes, a noticeable red shift of 24 nm was observed for the characteristic plasmonic band in the UV-Vis spectra (at 523 nm), which confirmed the formation of a real heterostructure between the FeS_2 and Au. Later, the intensity decreased as the overgrowth of the Au and FeS_2 increased (Fig. S13†). The PEC activity of AFS1.5 isolated after 15 min is much lower in comparison with AFS1.5 isolated at 3 min. Indeed, it is clear from the activities of the AFS2.5 and AFS1.5 (isolated at 15 min) that over growth led to self-aggregation of the FeS_2, which played a detrimental role in passivating the active surface species in the FeS_2 nanosheets. The optimized cathodic performance is very competitive compared with the highly efficient HER Pt catalyst on a planar p-type Si surface, which was recently shown to be one of the best buried-Si junction model systems.[60] We have also compared the activity of the FeS_2 and Au–FeS_2 heterostructures with several sulfide- and Pt-based electrocatalysts (Table S1†).

The wavelength-dependent incident photon-to-current conversion efficiency (IPCE) was measured for the Si/FeS_2 and Au–FeS_2 photocathodes connected to the photoelectrochemical system at wavelengths of 300–1000 nm. The IPCE value was extracted on the basis of the chronoamperometric current density (at 0 V) recorded at different wavelengths and compared with that of Au/Si as the control (Fig. 4e, S14†). The efficiency due to charge separation around the Si/FeS_2 interface covers the whole visible and short near-IR regions. Moreover, the favorable plasmonic hot electron injection could essentially fall under the background of typical broad light absorption of Si, which impacts the overall efficiency.[61,62] The order for photo-conversion efficiency is AFS1.5 > AFS2.5 > FS2.5 > FS1.5 > AFS0.5 > FS0.5, with the maximum (64%) achieved by AFS1.5. To gain a clear understanding of the PEC activity and the feasibility for charge transfer on the different photocathodes, an impedance study was also carried out at 0 V. The Nyquist plot shows that all the photocathodes have a single semicircle and the data

Published on 27 June 2019. Downloaded by Korea Advanced Institute of Science & Technology / KAIST on 1/16/2020 12:43:40 AM.

can be fitted to an equivalent circuit by ignoring minor diffusion of the catalysts (Fig. 4f). The circuit consists of constant-phase element for Si, FeS_2 (or Au-FeS_2), and W_o (the Warburg constant). The parameters R2 ($R_{ct,si}$) and R3 ($R_{ct,cat}$) signify the charge transfer resistance active at the Si/catalyst and the catalyst/electrolyte interfaces, respectively. As shown in the Nyquist plots for the Si/AFS1.5 electrode (Fig. S15†), the diameter of the semicircle is significantly smaller under light irradiation than in the dark, indicating that the photoinduced charge transferred through the electrode/electrolyte interface. Moreover, comprehensive evaluation of the different Si/FeS_2 or Au–FeS_2 catalysts exhibited an increase in charge transfer as the semicircle diameter decreased. The evaluated resistance values from the equivalent circuit of the photocathodes are tabulated in Table S2.† $R_{ct,si}$ were found to be slightly different for the different photocathodes. However, a larger decrease in $R_{ct,cat}$ can be seen for the Au heterostructures than that for the pure FeS_2 catalysts, which suggests that plasmons induce hot electrons in the Au that synergize the fast charge transfer around the catalyst/electrocatalyst interface.

To further illuminate the impact of varying the charge transfer efficiency into different FeS_2 catalyst surfaces, the solid-state photoluminescence (PL) property was examined for the as-deposited FeS_2 catalysts on a p-type Si surface using micro-PL/Raman spectroscopy. It is a potential tool for measuring the local charge carrier transport properties that are accompanied by traps or recombination of electrons, holes, and excitons inside the non-centrosymmetric materials with a direct band gap, which essentially circumvents the environmental species effect.[63–65] Radiative PL emission of pyrite FeS_2 originates from exciton recombination, where an excited electron recombines with a hole, resulting in the release of a photon in the process. High PL quantum yields indicate a higher recombination rate of electron–hole pairs and a longer lifetime of the PL state. FeS_2 has a sharp major emission peak centered at 459 nm, which is essentially caused by band-to-band transitions and depends on recombination of the photoexcited electrons.[66] Small features between 465 and 550 nm are attributed to different excitonic peaks in the sample, possibly caused by the Si. A gradual increase in the PL intensity from FS0.5 to FS2.5 was caused by the majority charge carrier to be relaxed *via* radiative recombination of the produced excitons (Fig. 5a). The results indicate that, under photoexcitation, the charge carrier transfer undoubtedly increased trough the Si/FS2.5 heterojunction. Moreover, it was suggested from the increased radiative recombination seen in an electron-dominated carrier-transfer process that the radiative lifetime of the electron acceptor will become longer while that of the electron donor will be correspondingly shorter.[67] Indeed, the time-dependent carrier decay profile was collected and the lifetime was measured at the observed PL maxima (Fig. 5b). By fitting with the second-order component, the calculated average lifetimes for FS0.5, FS1.5, and FS2.5 are 0.29, 0.32, and 0.41 ns, respectively. If the influence of any inverted impurities in the sample is excluded during solution processing, this accelerated PL decay dynamic can be attributed to long carrier diffusion and slow surface recombination,[68] which are likely a function of the 2D lateral growth of the FeS_2 catalysts (Fig. 5c).

The prime role of Au for increasing the catalytic efficiency by injecting hot carriers into the FeS_2 surface was investigated by characterizing the electronic features of the FeS_2 and Au–FeS_2 nanostructures (here FS1.5 and AFS1.5 were chosen as representative catalysts for convenience in the comparison). Because of the difference in the work functions of FeS_2 and Au, a built-in electric field can form across the heterojunction. This has been corroborated by local charge transfer observed in the XPS analysis. The Au 4f XPS peak shifted 0.23 eV lower towards the BE value in the Au–FeS_2 heterostructure (AFS1.5) compared with

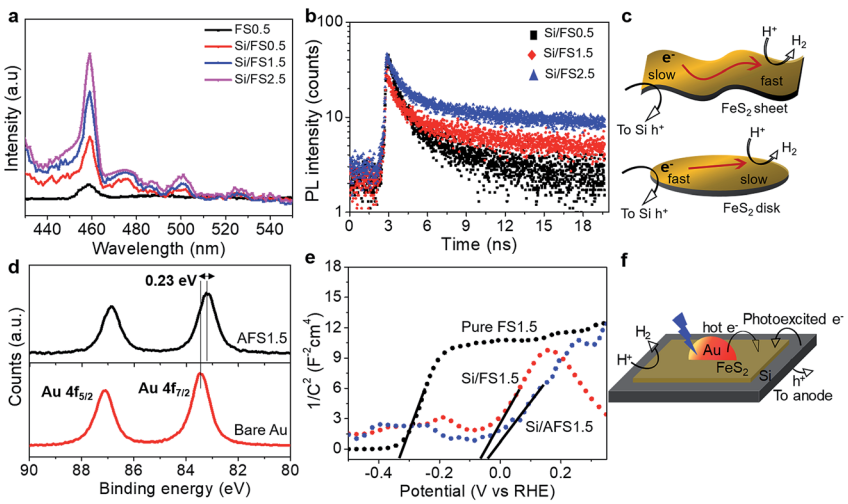

Fig. 5 (a) Micro PL/Raman spectra and (b) PL lifetime decays for the different FeS_2 nanostructures deposited on p-type Si. (c) Plausible working mechanism for the varied activity of the FeS_2 catalysts. (d) Au 4f XPS profile of the bare Au and the Au–FeS_2 heterostructure (AFS1.5). (e) Mott–Schottky plot of the different photocathodes performing under light irradiation ($1/C^2$ are on the order of 10^{12} and 10^{11} for FS2.5 and AFS1.5, respectively, and the estimated slopes are 49.18×10^{12} and 42.88×10^{11} F^2 cm^4 V^{-1} for FS2.5 and AFS1.5, respectively). (f) Plausible working mechanism for the Au–FeS_2 catalyst.

 This journal is © The Royal Society of Chemistry 2019

Published on 27 June 2019. Downloaded by Korea Advanced Institute of Science & Technology / KAIST on 1/16/2020 12:43:40 AM.

pure Au (Fig. 5d). However, the Fe^{2+} peak in the Fe 2p XPS profile shows no shift before or after the heterojunction formation (Fig. S7a and c†). This phenomenon caused by local charge transfer is important in the metal/semiconductor or semiconductor/semiconductor heterojunctions.[69]

To investigate the stability of the photoelectrode, chronoamperometric performance of the FS2.5 and AFS1.5 was checked for almost 12 h at the potential where each respective catalyst reaches a current density of 10 mA cm^{-2}. The minor fluctuations in the current density are likely caused by intense bubbling of the H_2 gas. The current density for FS2.5 showed a monotonic decrease after 250 min (Fig. S15†). This was possibly caused by dissolution of the S species from the electrode. However, the current density value is consistent for AFS1.5 and exhibited slow instability compared with FS2.5. The morphologies of the FS2.5 and AFS1.5 after the stability check did not deteriorate, as confirmed by TEM analysis of the catalysts after the reaction (Fig. S16b and c†). It is worth noting here that the scanning potential range and the current density passing through the electrode could not possibly have a detrimental influence on Pt dissolution. The XPS of the working electrode after the reaction (AFS1.5/Si), did not show any signal in the Pt 4f profile (Fig. S17†).

The energetics of the FeS_2 (pure and in the Au–FeS_2 heterostructure) at the Schottky junction were evaluated using Mott–Schottky analysis.[70,71] The flat band potential (E_{fb}) was estimated by taking the intercept of the extrapolated linear region at the minimum inverse square region capacitance (Fig. 5e). The measured E_{fb} of FS1.5 and AFS1.5 are very close (−0.053 and −0.027 V, respectively), which confirms that the Au did not have a major influence on the FeS_2 energetics (similar to the XPS observation). Moreover the p-type Si has an E_{fb} value of 0.47 V (*vs.* RHE) with a negative slope in the Mott–Schottky plot (Fig. S18†). Pure FeS_2 is n-type and displayed a positive slope with an estimated flat band potential of −0.33 V, which corroborates well with the reported experimental value.[72] The E_{fb} of the FS1.5 deposited on the Si electrode (−0.09 V *vs.* RHE) had a significant positive shift in comparison to pure FeS_2 (as FS1.5) deposited on FTO. The results clearly indicate the successful formation of a p–n type heterojunction. Subsequently, the donor density (N_d) was estimated by evaluating the slope of the curve from

$$\frac{1}{C^2} = \frac{2}{e\varepsilon\varepsilon_0 N_d}\left(E - E_{fb} - \frac{k_b T}{e}\right) \quad (1)$$

where N_d is the donor density, ε_0 is permittivity of the vacuum, ε is the dielectric constant of the semiconductor, E is the applied potential, E_{fb} is the flat-band potential, e is the electronic charge, K_b is Boltzmann's constant, and T is the absolute temperature.

It is interesting to note that after the inclusion of Au, the donor density (N_d) on the FeS_2 layer increased notably; the calculated N_d of FeS_2 in FS1.5 and AFS1.5 are 2.45×10^{17} and 2.81×10^{18} cm^{-3}, respectively. Indeed, it is clear that the overall efficiency of the Si/Au–FeS_2 photodevice is enhanced multiple times than that of the Si/FeS_2 device either by realizing multiple reflections between the double Schottky barrier tandem structure or by countering the ohmic losses using the metallic nature of the Au nanoparticle.[73,74] Notwithstanding, the contribution from plasmon-induced hot electrons is of central interest and might surpass the influence of other factors considered in earlier studies because all the experiments were carried out under white light irradiation. Thus, to provide incontrovertible evidence, chronoamperometric analysis was performed on the Au–FeS_2(AFS1.5)/FTO using a 650 nm 100 mW cm^{-2} laser pointer with chopped illumination. The experiment clearly shows enhancement of the current when the laser is on (Fig. S19†). This signifies the role of the Au nanoparticles in injecting hot electrons into the FeS_2 surface that eventually take part in the synergistic cathodic performance with the Si photoabsorber, albeit the FeS_2 surface is the reaction site.

Conclusions

In conclusion, we developed a novel hot-injection method to synthesize two-dimensional thin FeS_2 and its analogue Au heterostructures. The chemistry of the lateral growth for pyrite FeS_2 and the Au–FeS_2 modulated heterojunction are investigated based on their epitaxial relationship. On evaluating the photoelectrocatalytic performance of the as-prepared catalysts, we found that FeS_2 with micron-scale lateral growth is highly efficient, with a maximal minority carrier lifetime compared with other FeS_2 nanostructures. After plasmonic Au coupling, the Au–FeS_2 heterostructure also showed improved performance with an anodic shift of 0.25 V to generate a photocurrent of 10 mA cm^{-2} with considerable structural stability. The results also imply that FeS_2 as an electrocatalyst is also capable of carrying and transferring hot electrons that are generated from light irradiation. The predominant influence of changing the S^{2-} concentration for engineering the FeS_2 growth in either the pure state or in the heterojunction provided a clear view for preparing earth-abundant chalcogenides as more-efficient candidates for solar water splitting.

Experimental section

Synthesis of FeS_2 with different lateral growth

Thin FeS_2 nanostructures with different lateral growth were synthesized using the hot-injection method. In a typical synthesis, 35.3 mg (0.1 mmol) of iron(III) acetylacetonate (Wako Chemicals, 99.9%) and 2 g (8.3 mmol) of dodecylamine (Aldrich, 98%) were loaded in a three-necked flask and heated to 110 °C. The solution was first slowly evacuated, and then degassed under Ar flow for 15 min. 0.5 mL of trioctylphosphine (Aldrich, 97%) was then slowly injected into the three-necked flask. Immediately, the temperature of the reaction system was increased to 170 °C. The different sulfide sources were prepared in separate glass vials by dissolving 0.5 mmol (38.06 mg), 1.5 mmol (114.2 mg), or 2.5 mmol (190.3 mg) of thiourea (Aldrich, ≥99.0%) in 2 g (8.3 mmol) of dodecylamine at 100 °C with subsequent Ar purging. After digesting the iron(III) acetylacetonate at 170 °C for 15 min, the color of the solution turned dark brown, which confirms the formation of Fe^0. The sulfide source was then immediately injected into the reaction flask,

Published on 27 June 2019. Downloaded by Korea Advanced Institute of Science & Technology / KAIST on 1/16/2020 12:43:40 AM.

resulting in the formation of a completely black solution, which indicates the formation of FeS_2 sheets. The reaction was stopped after 15 min and the products were purified using chloroform as the solvent and acetone as the nonsolvent.

Synthesis of Au–FeS_2 heterostructure with different lateral growth

In the synthesis of the Au–FeS_2, the growth of the FeS_2 was stopped 2 min after adding the sulfide source by swiftly injecting 2 mL of a thoroughly Ar-purged 0.05 mmol $HAuCl_4$ solution in olylamine (prepared in a separate vial) into the FeS_2 growth solution and heated at 170 °C for 3 min. After stopping the reaction, the products were purified using chloroform as the solvent and acetone as the nonsolvent.

Fabrication of the Si-based working electrode

For all the photoelectrochemical measurements, p-type Si (resistance of 5–10 Ω.cm; 650–390 μm thick) was cut into small pieces (approximately 1 cm^2). These pieces were then treated under sonication using a 0.5 M aqueous HF solution followed by washing with deionized water and drying under Ar flow. Before preparing the catalyst ink, different FeS_2 and Au–FeS_2 nanostructures are treated for ligand exchange with a few drops of a sodium sulfide DMF mixture, and then washed with acetone. All the final products were suspended in 2 mL of chloroform and 500 μL of olylamine. The catalyst ink was prepared by dispersing 200 μL of the catalyst suspension into 800 μL of acetone. The resulting dispersion was drop casted (∼100 μL) onto the Si wafer pieces and spin coated at 3000 rpm. Finally, one drop of the 0.5% Nafion solution (in ethanol) was placed on the deposited catalyst followed by annealing at 150 °C for 1 h. In–Ga eutectics were then rubbed onto the back of the Si slices to create the ohmic contacts. Cu wire was rubbed onto the In–Ga eutectics and used as the external connection. The whole back and edges of the Si/catalyst slices were sealed with epoxy resin to isolate the working electrode from the electrolyte.

Electrochemical and photoelectrochemical experiments

All the electrochemical and photoelectrochemical measurements were carried out using a multichannel potentiostat (VersaStat3, Princeton Applied Research, USA) electrochemical workstation featuring a three-electrode cell with a Pt wire (counter), Ag/AgCl reference, and p-Si/FeS_2 (or Au–FeS_2) working electrode. The photoresponse was recorded while under continuous irradiation from a 150 W Xe lamp (Model 10500, ABET Technology). A monochromator (Mmac 200, Dongwoo OPTRON) at 300–900 nm was used during the IPCE measurements. The intensity of the light was calibrated using an irradiatometer (ADCMT optical power meter) to simulate AM 1.5 illumination (100 mW cm^{-2}). All the reactions were performed in a 0.2 M H_2SO_4 solution. Before using the electrolyte solution for the photoelectrochemical reaction, it was purged with pure Ar for 30 min to eliminate any dissolved oxygen. Unless indicated, all the potentials were calibrated to the reversible hydrogen electrode (RHE) according to the following equation.

$$E(V\ vs.\ \mathrm{RHE}) = E(V\ vs.\ \mathrm{Ag/AgCl}) + 0.1976 + 0.0591\ \mathrm{pH} \quad (2)$$

The Mott–Schottky plots were obtained at a frequency of 1 KHz with a step size greater than 40 (adjusted) to determine the flat-band potential. The electrochemical impedance spectroscopy measurements were carried out in the dark and with light irradiation at an applied voltage of 0.0 V *vs.* RHE with the frequency ranging from 0.1 to 100 KHz. The fill factor (ff) was calculated using $\mathrm{ff} = (I_{mp} \times V_{mp})/(I_{sc} \times V_{oc})$ where I_{mp} is the externally measured current density at a particular voltage V_{mp} and I_{sc} is the short-circuit current close to the open circuit potential V_{oc}.

Conflicts of interest

The authors declare no conflict of interest.

Acknowledgements

This work was supported by the Institute for Basic Science (IBS) [IBS-R004].

References

1 D. G. Schmidt, *ACS Energy Lett.*, 2016, **1**, 244.
2 F. Li, J. Li, F. Li, L. Gao, X. Long, Y. Hu, C. Wang, S. Wei, J. Jin and J. Ma, *J. Mater. Chem. A*, 2018, **6**, 13412–13418.
3 B. Naik, S. M. Kim, C. H. Jung, S. Y. Moon and J. Y. Park, *Adv. Mater. Interfaces*, 2014, **1**, 1300018.
4 T. Yao, X. An, H. Han, J. Q. Chen and C. Li, *Adv. Energy Mater.*, 2018, **8**, 1800210.
5 J. Li, P. Zhou, F. Li, R. Ren, Y. Lu, J. Niu, J. Ma, X. Zhang, M. Tian, J. Jin and J. Ma, *J. Mater. Chem. A*, 2015, **3**, 11261–11268.
6 I. Mondal, S. Y. Moon, H. Kim and J. Y. Park, *Int. J. Hydrogen Energy*, 2019, **44**, 7241–7251.
7 Y. Hikita, K. Nishio, L. C. Seitz, P. Chakthranont, T. Tachikawa, T. F. Jaramillo and H. Y. Hwang, *Adv. Energy Mater.*, 2016, **6**, 1502154.
8 L. C. Seitz, Z. Chen, A. J. Forman, B. A. Pinaud, J. D. Benck and T. F. Jaramillo, *ChemSusChem*, 2014, **7**, 1372–1385.
9 K. Sun, S. Shen, Y. Liang, P. E. Burrows, S. S. Mao and D. Wang, *Chem. Rev.*, 2014, **114**, 8662–8719.
10 M. J. Kenney, M. Gong, Y. Li, J. Z. Wu, J. Feng, M. Lanza and H. Dai, *Science*, 2013, **342**, 836–840.
11 M. Ledendecker, J. S. Mondschein, O. Kasian, S. Geiger, D. Göhl, M. Schalenbach, A. Zeradjanin, S. Cherevko, R. E. Schaak and K. Mayrhofer, *Angew. Chem., Int. Ed.*, 2017, **56**, 9767–9771.
12 X. Yao Yu and X. W. (David) Lou, *Adv. Energy Mater.*, 2017, **8**, 1701592.
13 S. Anantharaj, S. R. Ede, K. Sakthikumar, K. Karthick, S. Mishra and S. Kundu, *ACS Catal.*, 2016, **6**, 8069–8097.
14 J. Su, Y. Wei and L. Vayssieres, *J. Phys. Chem. Lett.*, 2017, **8**, 5228–5238.

 This journal is © The Royal Society of Chemistry 2019

Published on 27 June 2019. Downloaded by Korea Advanced Institute of Science & Technology / KAIST on 1/16/2020 12:43:40 AM.

15 C. Panda, P. W. Menezes, C. Walter, S. Yao, M. E. Miehlich, V. Gutkin, K. Meyer and M. Driess, *Angew. Chem., Int. Ed.*, 2017, **56**, 10642–10646.
16 Y. Hou, M. Qiu, G. Nam, M. G. Kim, T. Zhang, K. Liu, X. Zhuang, J. Cho, C. Yuan and X. Feng, *Nano Lett.*, 2017, **17**, 4202–4209.
17 L. Gao, F. Li, H. Hu, X. Long, N. Xu, Y. Hu, S. Wei, C. Wang, J. Ma and J. Jin, *ChemSusChem*, 2018, **11**, 2502–2509.
18 N. Mahmood, Y. Yao, J.-W. Zhang, L. Pan, X. Zhang and J.-J. Zou, *Adv. Sci.*, 2018, **5**, 1700464.
19 T. D. Thanh, N. D. Chuong, H. V. Hien, T. Kshetri, L. H. Tuan, N. H. Kim and J. H. Lee, *Prog. Mater. Sci.*, 2018, **96**, 51–85.
20 Q. Lu, Y. Yu, Q. Ma, B. Chen and H. Zhang, *Adv. Mater.*, 2016, **28**, 1917–1933.
21 X. Yu, M. S. Prévot, N. Guijarro and K. Sivula, *Nat. Commun.*, 2015, **6**, 7596.
22 F. Wang, T. A. Shifa, X. Zhan, Y. Huang, K. Liu, Z. Cheng, C. Jiang and J. He, *Nanoscale*, 2015, **7**, 19764–19788.
23 D. E. -López, Z. Lou and N. V. Rees, *Adv. Energy Mater.*, 2019, 1802614.
24 C.-Y. Lin, D. Mersch, D. A. Jefferson and E. Reisner, *Chem. Sci.*, 2014, **5**, 4906–4913.
25 Y. Sun, C. Liu, D. C. Grauer, J. Yano, J. R. Long, P. Yang and C. J. Chang, *J. Am. Chem. Soc.*, 2013, **135**, 17699–17702.
26 Z. Li and Z. Zhang, *Nano Res.*, 2018, **11**, 1530–1540.
27 K. Ren, P. Yin, Y. Zhou, X. Cao, C. Dong, L. Cui, H. Liu and X. Du, *Small*, 2017, **13**, 1700867.
28 P. Chen, T. Zhou, M. Zhang, Y. Tong, C. Zhong, N. Zhang, L. Zhang, C. Wu and Y. Xie, *Adv. Mater.*, 2017, **29**, 1701584.
29 P. Luo, H. J. Zhang, L. Liu, Y. Zhang, J. Deng, C. H. Xu, N. Hu and Y. Wang, *ACS Appl. Mater. Interfaces*, 2017, **9**, 2500–2508.
30 D. A. Reddy, H. Park, R. Ma, D. P. Kumar, M. Lim and T. K. Kim, *ChemSusChem*, 2017, **10**, 1563–1570.
31 M. Tabata, K. Maeda, T. Ishihara, T. Minegishi, T. Takata and K. Domen, *J. Phys. Chem. C*, 2010, **114**, 11215–11220.
32 C. Di Giovanni, W.-A. Wang, S. Nowak, J.-M. Greneche, H. Lecoq, L. Mouton, M. Giraud and C. Tard, *ACS Catal.*, 2014, **4**, 681–687.
33 D. Jasion, J. M. Barforoush, Q. Qiao, Y. Zhu, S. Ren and K. C. Leonard, *ACS Catal.*, 2015, **5**, 6653–6657.
34 R. Miao, B. Dutta, S. Sahoo, J. He, W. Zhong, S. A. Cetegen, T. Jiang, S. P. Alpay and S. L. Suib, *J. Am. Chem. Soc.*, 2017, **139**, 13604–13607.
35 Y. Li, J. Yin, L. An, M. Lu, K. Sun, Y. Q. Zhao, D. Gao, C. Fangyi and P. Xi, *Small*, 2018, **14**, 1801070.
36 X. Zou, Y. Wu, Y. Liu, D. Liu, W. Li, L. Gu, H. Liu, P. Wang, L. Sun and Y. Zhang, *Chem*, 2018, **4**, 1139–1152.
37 S. Y. Moon, H. C. Song, E. H. Gwag, I. I. Nedrygailov, C. Lee, J. J. Kim, W. H. Doh and J. Y. Park, *Nanoscale*, 2018, **10**, 22180–22188.
38 G. Liu, P. Li, G. Zhao, X. Wang, J. Kong, H. Liu, H. Zhang, K. Chang, X. Meng, T. Kako and J. Ye, *J. Am. Chem. Soc.*, 2016, **138**, 9128–9136.
39 N. Xu, F. Li, L. Gao, H. Hu, Y. Hu, X. Long, J. Ma and J. Jin, *ACS Sustainable Chem. Eng.*, 2018, **6**, 7257–7264.
40 K. Büker, N. Alonso-Vante and H. Tributsch, *J. Appl. Phys.*, 1992, **72**, 5721–5728.
41 M. Cargnello, *Chem. Mater.*, 2019, **31**, 576–596.
42 S. A. McCarthy, R. Ratkic, F. Purcell-Milton, T. S. Perova and Y. K. Gun'ko, *Sci. Rep.*, 2018, **8**, 2860.
43 S. Mourdikoudis and L. M. Liz-Marzan, *Chem. Mater.*, 2013, **25**, 1465–1476.
44 S. Jana, B. B. Srivastava and N. Pradhan, *J. Phys. Chem. C*, 2012, **117**, 1183–1188.
45 L. Peng, P. Xiong, L. Ma, Y. Yuan, Y. Zhu, D. Chen, X. Luo and J. Lu, *Nat. Commun.*, 2017, **8**, 15139.
46 B. Yuan, W. Luan, S.-T. Tu and J. Wu, *New J. Chem.*, 2015, **39**, 3571–3577.
47 H. Yang, A. Giri, S. Moon, S. Shin, J.-M. Myoung and U. Jeong, *Chem. Mater.*, 2017, **29**, 5772–5776.
48 H. Yu, M. Chen, P. M. Rice, S. X. Wang, R. L. White and S. Sun, *Nano Lett.*, 2005, **5**, 379–382.
49 M. Rahaman, R. D. Rodriguez, G. Plechinger, S. Moras, C. Schüller, T. Korn and D. R. T. Zahn, *Nano Lett.*, 2017, **17**, 6027–6033.
50 A. Figuerola, M. V. Huis, M. Zanella, A. Genovese, S. Marras, A. Falqui, H. W. Zandbergen, R. Cingolani and L. Manna, *Nano Lett.*, 2010, **10**, 3028–3036.
51 R. Bose, A. H. M. Abdul Wasey, G. P. Das and N. Pradhan, *J. Phys. Chem. Lett.*, 2014, **5**, 1892–1898.
52 D. Susac, L. Zhu, M. Teo, A. Sode, K. C. Wong, P. C. Wong, R. R. Parsons, D. Bizzotto, K. A. R. Mitchell and S. A. Campbell, *J. Phys. Chem. C*, 2007, **111**, 18715–18723.
53 C. Acevedo, M. J. Shearer, K. Park, R. J. Hamers and S. Jin, *Chem. Mater.*, 2015, **27**, 3108–3114.
54 M. Cargnello, C. Chen, B. T. Diroll, V. V. T. Doan-Nguyen, R. J. Gorte and C. B. Murray, *J. Am. Chem. Soc.*, 2015, **137**, 6906.
55 J. R. McKone, N. S. Lewis and H. B. Gray, *Chem. Mater.*, 2014, **26**, 407–414.
56 M. G. Walter, E. L. Warren, J. R. McKone, S. W. Boettcher, Q. Mi, E. A. Santori and N. S. Lewis, *Chem. Rev.*, 2010, **110**, 6446–6473.
57 J. Gu, J. A. Aguiar, S. Ferrere, K. X. Steirer, Y. Yan, C. Xiao, J. L. Young, M. A. Jassim, N. R. Neale and J. A. Turner, *Nat. Energy*, 2017, **2**, 16192.
58 Q. Li, M. Zheng, M. Zhong, L. Ma, F. Wang, L. Ma and W. Shen, *Sci. Rep.*, 2016, **6**, 29738.
59 F. Urbain, V. Smirnov, J.-P. Becker, A. Lambertz, F. Yang, J. Ziegler, B. Kaiser, W. Jaegermann, U. Rau and F. Finger, *Energy Environ. Sci.*, 2016, **9**, 145–154.
60 Z. Yin, R. Fan, G. Huang and M. Shen, *Chem. Commun.*, 2018, **54**, 543–546.
61 D. Bae, B. Mei, R. Frydendal, T. Pedersen, B. Seger, O. Hansen, P. C. K. Vesborg and I. Chorkendorff, *ChemElectroChem*, 2016, **3**, 1546–1552.
62 C.-J. Chen, M.-G. Chen, C. K. Chen, P. C. Wu, P.-T. Chen, M. Basu, S.-F. Hu, D. P. Tsai and R.-S. Liu, *Chem. Commun.*, 2015, **51**, 549–552.
63 K. F. Mak, K. He, C. Lee, G. H. Lee, J. Hone, T. F. Heinz and J. Shan, *Nat. Mater.*, 2013, **12**, 207–211.

Published on 27 June 2019. Downloaded by Korea Advanced Institute of Science & Technology / KAIST on 1/16/2020 12:43:40 AM.

64 S. Tongay, J. Suh, C. Ataca, W. Fan, A. Luce, J. S. Kang, J. Liu, C. Ko, R. Raghunathanan, J. Zhou, F. Ogletree, J. Li, J. C. Grossman and J. Wu, *Sci. Rep.*, 2013, **3**, 2657.

65 A. Alarawi, V. Ramalingam, H.-C. Fu, P. Varadhan, R. Yang and J.-H. He, *Opt. Express*, 2019, **27**, A352–A356.

66 S. Khalid, M. A. Malik, D. J. Lewis, P. Kevin, E. Ahmed, Y. Khan and P. O'Brien, *J. Mater. Chem. C*, 2015, **3**, 12068–12076.

67 W. Xu, W. Liu, J. F. Schmidt, W. Zhao, X. Lu, T. Raab, C. Diederichs, W. Gao, D. V. Seletskiy and Q. Xiong, *Nature*, 2017, **541**, 62–67.

68 B. Wu, Y. Zhou, G. Xing, Q. Xu, H. F. Garces, A. Solanki, T. W. Goh, N. P. Padture and T. C. Sum, *Adv. Funct. Mater.*, 2017, **27**, 1604818.

69 H. Henck, Z. B. Aziza, O. Zill, D. Pierucci, C. H. Naylor, M. G. Silly, N. Gogneau, F. Oehler, S. Collin, J. Brault, F. Sirotti, F. S. Bertran, P. L. Fèvre, S. Berciaud, A. T. C. Johnson, E. l. Lhuillier, J. E. Rault and A. Ouerghi, *Phys. Rev. B*, 2017, **96**, 115312.

70 X. Zhou, R. Liu, K. Sun, K. M. Papadantonakis, B. S. Brunschwig and N. S. Lewis, *Energy Environ. Sci.*, 2016, **9**, 892–897.

71 I. A. Digdaya, G. W. P. Adhyaksa, B. J. Trześniewski, E. C. Garnett and W. A. Smith, *Nat. Commun.*, 2017, **8**, 15968.

72 M. Barawi, I. J. Ferrer, E. Flores, S. Yoda, J. R. Ares and C. Sánchez, *J. Phys. Chem. C*, 2016, **120**, 9547–9552.

73 G. Liu, P. Li, G. Zhao, X. Wang, J. Kong, H. Liu, H. Zhang, K. Chang, X. Meng, T. Kako and J. Ye, *J. Am. Chem. Soc.*, 2016, **138**, 9128–9136.

74 Y. K. Lee, H. Lee and J. Y. Park, *Sci. Rep.*, 2014, **4**, 4580.

 This journal is © The Royal Society of Chemistry 2019